Synthetic radio maps of CME-driven shocks below 4 solar radii heliocentric distance

J. M. Schmidt[1] and N. Gopalswamy[1]

[1]   We present 2 1/2 D numerical MagnetoHydroDynamic (MHD) simulations of coronal mass ejections (CMEs) in conjunction with plasma simulations of radio emission from the CME-driven shocks. The CME-driven shock extends to an almost spherical shape during the temporal evolution of the CME. Our plasma simulations can reproduce the dynamic spectra of coronal type II radio bursts, with the frequency drift rates corresponding to the shock speeds. We find further, that the CME-driven shock is an effective radio emitter at metric wavelengths, when the CME has reached a heliocentric distance of about two solar radii ($R_\odot$). We apply our simulation results to explain the radio images of type II bursts obtained by radio heliographs, in particular to the banana-shaped images of radio sources associated with fast CMEs.

1.   Introduction

[2]   Coronal Mass Ejections (CMEs) are widely recognized as major transient events that carry away mass and momentum from the corona of the Sun [e.g., *Hundhausen*, 1999]. CME speeds at the Sun can lie anywhere between less than 100 and in excess of 3000 km/s, and their masses can be as large as 10^{16} g [*Hundhausen*, 1999; *St. Cyr et al.*, 2000; *Gopalswamy*, 2006]. CMEs are imaged by coronagraphs [*Hundhausen et al.*, 1984] such as the Large Angle Spectrometric COronagraph (LASCO) [*Brueckner et al.*, 1995] on the Solar and Heliospheric Observatory (SoHO). They can also be observed as interplanetary CMEs (ICMEs) by spacecraft in situ [e.g., *Klein and Burlaga*, 1982; *Sheeley et al.*, 1985; *Crooker et al.*, 1997]. When CMEs move faster than the local Alfvén speed, they drive shocks which in turn accelerate electrons that produce type II radio bursts. From the starting frequency of metric type II bursts, and CME height-time plots it is found that the shock forms typically when the CME is at a heliocentric distance $<2~R_\odot$ [e.g., *Gopalswamy et al.*, 2005]. Unfortunately, this region of the corona is rarely imaged. For example, the LASCO coronagraphs C2 telescope images from 2.2 $R_\odot$ onwards. LASCO/C1 had a better field of view (fov) starting from 1.1 $R_\odot$, but it operated only for a short time. STEREO/COR1 has an fov in the range 1.4–4 $R_\odot$, but currently it is solar minimum with very few type II bursts from the Sun. Moreover, fast CMEs traverse the inner corona quickly, so the image cadence is usually not sufficient to capture the details of CME structure. A precise prediction of the behavior of CMEs in interplanetary space also requires a proper knowledge of the physical properties of CMEs in the solar corona below a heliocentric distance of $\sim$4 $R_\odot$ [see, e.g., *Gopalswamy et al.*, 2000].

[3]   Metric and kilometric type II radio bursts are interpreted as being caused by shock-accelerated electrons that generate radiation at the local plasma frequency and its second harmonic. The association between interplanetary (hectometric and kilometric) type II bursts and CME driven shocks is firmly established [*Cane et al.*, 1987]. *Reiner et al.* [1998] demonstrated unambiguously that interplanetary type II radio emission is generated upstream of the CME-driven shock. One of such radio facilities measuring type II radio emission is the radio receiver RAD2 of the WAVES experiment on board the Wind spacecraft, which measures between 1.075–13.825 MHz, or in decameter-hectometric (DH) wavelengths between 21–280 m [e.g., *Bougeret et al.*, 1995]. It is necessary to carry out these observations from spacecrafts, since radio signals below about 10 MHz, which correspond to heliocentric distances above about 2.3 $R_\odot$, cannot be observed from Earth because of the ionospheric absorption at these frequencies. However, single point spacecraft measurements cannot reveal the detailed spatial distribution of shock events.

[4]   Radio observations closer to the Sun are made by ground-based radio instruments. Radioheliographs image the corona close to the Sun, and hence can provide spatial information on radio bursts. For example, the Nançay radioheliograph images at five distinct frequencies between 164 MHz and 432 MHz. By correlating signals between spatially distributed antennas, spatially resolved radio maps of the solar corona can be obtained. The sharpness of the radio image can be improved by correlating more antennas. The LOw Frequency ARray (LOFAR) covers plasma frequencies at distances between approximately 1.3 and 2.3 $R_\odot$ from the Sun's center [*Röttgering et al.*, 2005]. The Mileura

[1]NASA Goddard Space Flight Center, Solar System Exploration, Greenbelt, Maryland, USA.
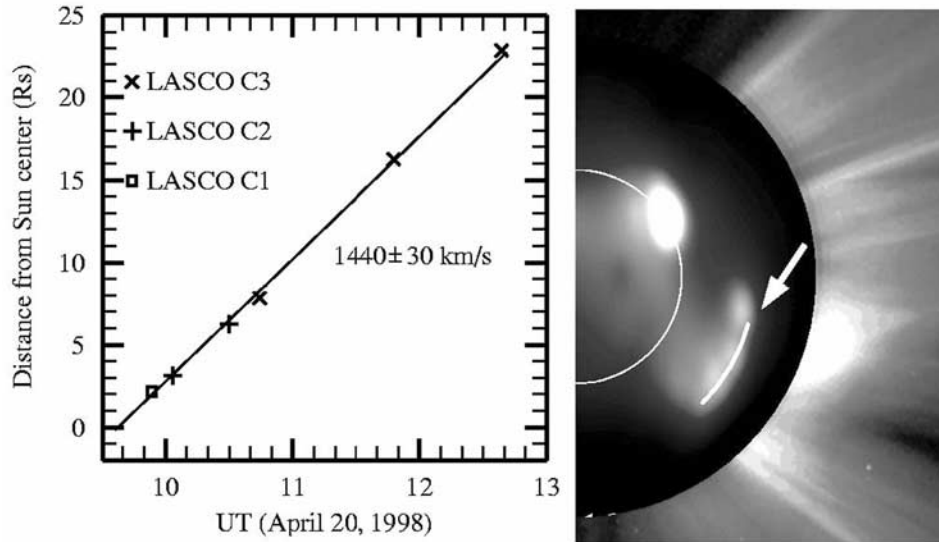
Figure 1. The shock front of a CME as a banana-shaped radio source as seen with the Nançay radioheliograph. The shock front (curved line, which is denoted by the arrow) is extrapolated to smaller heliocentric distances from LASCO observations. The shock has about 1.75 $R_\odot$ heliocentric distance, and the image was taken at 9:50 UT. It corresponds to a stage of the CME eruption shortly after the launch of the shock wave. The image is taken from *Maia et al.* [2000], reproduced by permission of the AAS.

Widefield Array (MWA) covers frequencies between 80–300 MHz with an equivalent fov [*Salah et al.*, 2005]. Both arrays have the capacity to map detailed CME events in radio light close to the Sun.

[5] For an interpretation of the observed signatures of a CME eruption in radio maps, the MHD modeling of a CME and kinetic modeling of the excited radio emission are needed. At present we are not capable to describe all relevant physical effects in one unified theory that comprises the very large scales of MHD theory and the very small scales of kinetic radiative effects. Yet, our approach presented here provides a step in the correct direction, since the energy released in the radiation is so small that it hardly influences the MHD system. We have performed such simulations and modeling that lead to synthetic radio maps of CMEs in the corona below $\sim$4 $R_\odot$ and discuss their physical properties in this work.

[6] The work is organized as follows: In section 2 we describe a tpye II burst imaged by the Nançay radioheliograph. Section 3 introduces an ideal MHD model for a CME in the solar corona. This model provides the large scale fields within a CME. Ideal MHD theory does not include kinetic plasma effects that can lead to radiation. These are described with small scale fluctuations of the fields, caused by particles in motion. The linkage between the large scale fields and the particle fluctuations, described with a distribution function, is provided with Vlasov's equation, where the large scale fields are coefficients. In specific resonant situations, the distribution function can grow to a delta peak like function, i.e., a particle beam is generated. Accelerated particles have plasma waves and ion sound waves as a consequence. These waves can interact with each other and with the background fields in a stochastical manner. In the course of these stochastical interactions, electromagnetic radio radiation is set free. All

those processes, from the growth of instabilities within Vlasov's theory to the stochastical growth of waves in a plasma, can be treated with analytical modeling. Section 4 develops the analytical kinetic model for the computation of the excited radio emission. A discussion of the spatial distribution and temporal evolution of the synthetic radio maps that we obtain can be found in section 5. In section 6 we draw our conclusions.

2. Radio Map Observation of a CME-Driven Shock

[7] On 20 April 1998, starting around 9:20 UT, the Nançay radioheliograph observed a succession of impulsive type III radio bursts in the southwest quadrant of the observational field. Following this activity, a weak banana-shaped radio source drifted in frequency and had no polarization, which are both characteristics of type II radio emission [see also *Nelson and Melrose*, 1985]. This source was first seen after 9:43 UT at 327 MHz and then at 236 MHz (at about 9:45 UT) and 164 MHz (from about 9:50 UT). This radio source was easy to distinguish from the background. It started as a very faint stationary source for a few tens of seconds, and then the flux at that position rose abruptly and the exciter of the source moved outward with an initial projected velocity of around 1000 km s^{-1}. If the source is assumed to start drifting at the arrival of the type II exciter, the onset times and positions at 236 and 164 MHz give an averaged velocity of 1200 $\pm$ 150 km s^{-1} for the exciter (for details see *Maia et al.* [2000]).

[8] From about 10:03 UT on, the LASCO images of the same event showed the progression of a CME in the C2 fov (the CME was also seen on a C1 image at 9:54 UT). Figure 1 (left) shows the position of the CME's leading edge as a
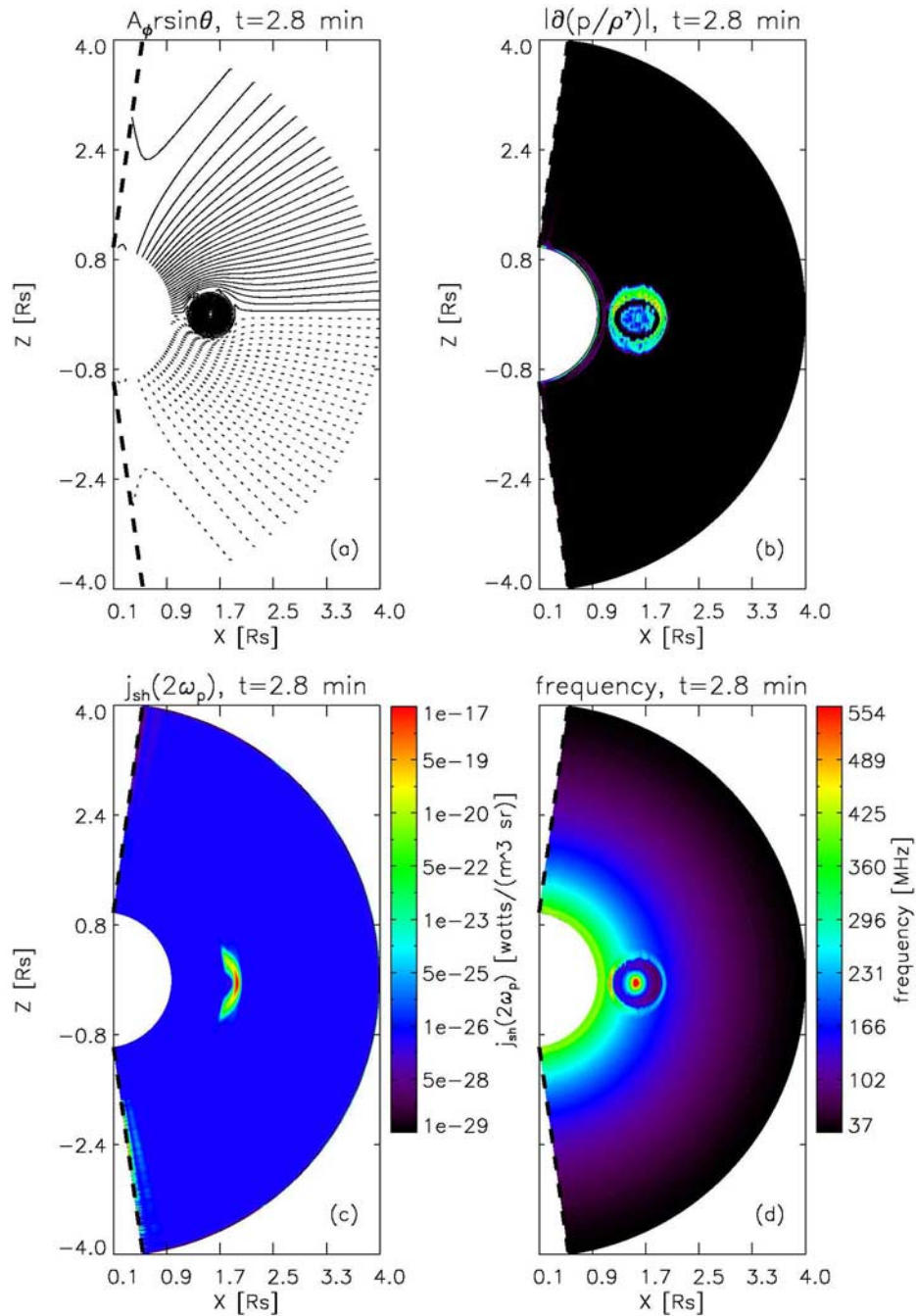
Figure 2. State of the CME at 2.8 min after the launch. The CME-driven shock develops. The shock area can be seen as a ring area of enhanced entropy gradient that surrounds the CME in Figure 2b. This ring area is an area of enhanced second harmonic plasma emission in Figure 2c, too. Maximum emissivities with $5 \times 10^{-22} - 1 \times 10^{-17}$ W m^{-3} sr^{-1} occur at the front edge of the shock, where there is the largest gradient of the magnetic field, as can be seen in the field line plot of Figure 2a. The emission frequency distribution in Figure 2d reveals that the outward propagating part of the CME's shock emits in a banana-shaped area at about 260 MHz.

function of time. The measured projected velocity for the CME's leading edge is 1440 ± 30 km s^{-1}, which agrees well with the measured value for the radio source. The catalog speed of this CME, averaged over the LASCO fov, is $\sim$1863 km s^{-1}. Using the velocity estimate and the position of the CME's leading edge in the 9:54 UT C1 LASCO image, *Maia et al.* [2000] extrapolated the leading edge position to about 1.75 $R_\odot$ at 9:50 UT, coinciding with the
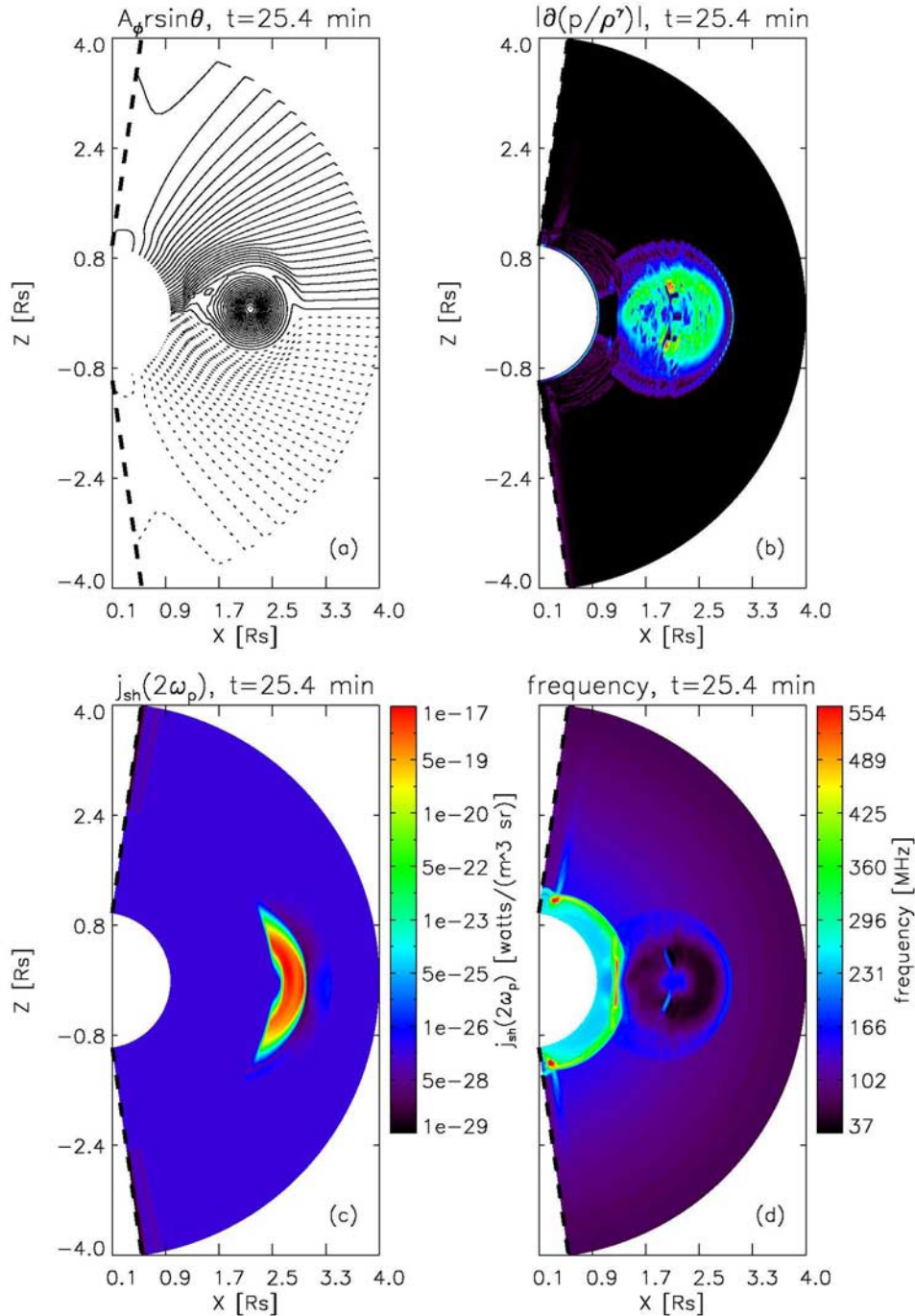
Figure 3. State of the CME at 25.4 min after the launch. The CME has grown in size considerably, and the shock front has reached almost 2.9 $R_\odot$ heliocentric distance. This shock front sharply defines the front border of the area of the CME that emits at about $5 \times 10^{-22} - 1 \times 10^{-17}$ W m^{-3} sr^{-1} in Figure 3c. Behind the shock, there is a rarefaction region of density in the direction toward the center of the CME, where the emission frequency decreases significantly, as can be seen in Figure 3d. Frequency-fixed receivers would see an eclipse of the radio signal in that direction.

type II radio source location at 164 MHz (see Figure 1 (right)). The estimated error in the extrapolated position is around ±0.05 $R_\odot$.

[9] *Maia et al.* [2000] conclude that the metric type II radio burst is likely the signature of a CME-driven shock.

Vourlidas et al. [1999] have identified four more examples (1 July, 19 August, and 24 December 1996 and 7 October 1997) of weak type II radio sources associated with the front of white-light CMEs. We substantiate the spatially distributed shock wave excitation of radio emission in a CME-
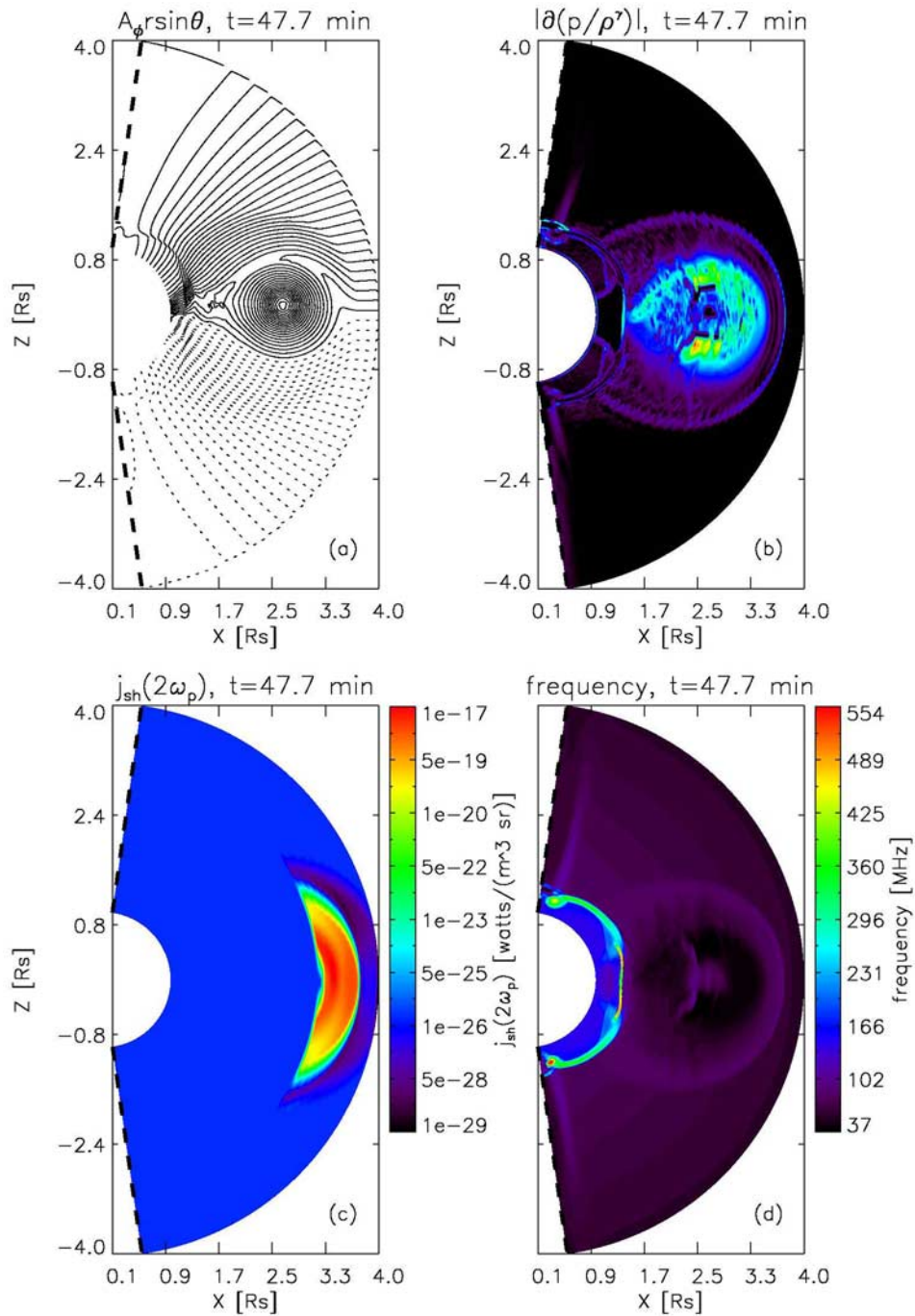
Figure 4. State of the CME at 47.7 min after the launch. The shock front of the CME has reached about 3.7 $R_\odot$ heliocentric distance. The emission frequency in the area behind the shock front, visible as an elongated banana-like radio source for frequency-fixed receivers, starts to decrease slowly.

driven shock by carrying out simulations as discussed in the following sections.

3. MHD Model

[10] The MHD code used is based on the algorithms described by *Zalesak* [1979] and *DeVore* [1991] for a flux-corrected transport (FCT) scheme for solving the MHD equations. It is fourth order in accuracy in space and second order in accuracy in time. In this code the magnetic field satisfies the divergence-free condition to machine accuracy. This code has been applied successfully to the description of the so-called over-expanding CMEs observed by Ulysses [*Cargill et al.*, 2000], the magnetic cloud evolution in a two-speed solar wind to explain Ulysses observations of parts of CMEs that separate [*Schmidt and Cargill*, 2001], the role of reconnection between CME and solar wind magnetic fields [*Schmidt and Cargill*, 2003], and colliding CMEs that

provide a very promising environment for particle acceleration [*Schmidt and Cargill*, 2004].

[11] FCT codes are well known for the sharpness of shocks. For example, Figure 5 by *Cargill et al.* [2000] shows sharp features of the magnetic field, velocity, density, pressure and plasma-β at the location of a shock. These are followed up to 5.6 AU. No artificial dissipation is used to stabilize the shock. The latter would quickly damp the shock, which would have an effect on the radio emission. In the version used here, the MHD equations are solved in spherical coordinates r, θ, where a rotational symmetry around the rotation axis z of the Sun is assumed, i.e., all fields are considered as being independent of the azimuthal coordinate ϕ. Yet, all vector fields have three components, i.e., the code is 2 1/2 dimensional. In the r-θ plane the computational grid consists of 300×100 points, where the radial extension of the simulation box is between one and four $R_\odot$. In our simulations, x denotes the radial in-ecliptic coordinate, and thick dashed lines in Figures 2, 3, and 4 denote the boundaries of the simulation box at $\theta = 9.7°$ and $\theta = 170.2°$.

[12] Boundary conditions are floating at the meridional sides and at 4 $R_\odot$. At 1 $R_\odot$ we fix the density, velocity, magnetic field and the pressure ρ, v, B and p of the solar wind. The current density j can be obtained using the curl of B. Specific numbers can be found in the discussion below. Of course, the simulation cannot include a detailed model of the small-scale photospheric fields. Instead, average values for velocity, magnetic field, pressure and number density are assumed at the inner boundary and in the volume of the simulation box. This assumption can be justified, since the CME eruption grows rapidly in size. Almost instantly, the CME covers a large volume, and its dynamics is controlled by the average fields over this volume. In particular, the solar wind is introduced as a radial Parker wind, which reaches a velocity of about 200 km s^{-1} at 4 $R_\odot$ heliocentric distance. This is in the same order as measurements of *Sheeley et al.* [1997], who found scattered velocity values around about 200 km s^{-1} for moving coronal features near 5 $R_\odot$ heliocentric distance in LASCO images. The pressure follows an adiabatic law with a polytropic index $\gamma = 5/3$. This law assumes a coronal temperature of 1.2 MK at 1 $R_\odot$ heliocentric distance and a number density $n_0(R_\odot) = 3.3 \times 10^8$ cm^{-3} for a Parker density profile, which are typical values for the solar corona [see, e.g., *Aschwanden*, 2004]. These values correspond to $p \approx 0.055$ dyne cm^{-2} and a double plasma frequency of about 326 MHz at 1 $R_\odot$ heliocentric distance.

[13] The CME is introduced as a flux rope of cylindrical shape that extends like a torus around the z axis embedded in an appropriately distorted radial solar magnetic field. This introduction of the CME is not a simple superposition on the ambient medium. We use an exact solution of the magnetostatic Maxwell equations described by *Schmidt* [2000] for this configuration. CMEs with a flux rope geometry are a subclass of observed CMEs [see, e.g., *Cremades and Bothmer*, 2004]. A summary of modeling efforts regarding CMEs that emerge from magnetic flux ropes or bubbles are discussed by *Forbes et al.* [2006]. Initially, the center of the flux rope is at 1.38 $R_\odot$ heliocentric distance in the ecliptic plane below the 1.75 $R_\odot$ heliocentric distance value for the initial shock observation of *Maia et al.* [2000]. The velocity and the diameter of the initial flux rope are 100 km s^{-1} and 0.61 $R_\odot$, respectively. The field strength of the solar magnetic field is highly variable at the inner boundary of the simulation box at one $R_\odot$ heliocentric distance. At $\theta = 9.7°$ and $\theta = 170.2°$ the magnetic field is 2 G at this boundary. The magnetic field grows along this boundary for angles θ that approach $\theta = 90°$. It has a peak value of 400 G at $\theta = 90°$ and a heliocentric distance of one $R_\odot$. These are typical values for foot point magnetic fields in active regions [see, e.g., *Aschwanden et al.*, 1999]. Within the simulation box, the magnetic field is appropriately distorted around the body of the CME, and it is divergent. Thus the average magnetic field strength is about 4 G around the body of the CME. The magnetic field has a value of 16 G along the symmetry axis in the middle of the flux rope. *Pneuman* [1984] demonstrated that a radial magnetic field with a strength of 4 G at 1 $R_\odot$ heliocentric distance, which surrounds a diamagnetic body with a larger magnetic field, accelerates this body to about 1800 km s^{-1} near 5 $R_\odot$ heliocentric distance within the gravitational field of the Sun [see his Figure 10]. The initial internal pressure of the CME is increased by a factor of three with respect to the external solar wind pressure. This assumption about the initial internal overpressure, which is unknown from the observations, leads to the observed sizes of CMEs in the interplanetary space [e.g., *Gosling et al.*, 1998], yet it does not dominate the dynamical evolution of the CME.

[14] Since ϕ is considered to be constant in this 2 1/2 D model, a torus-shaped geometry is maintained throughout the simulation. If the CME had foot points at the solar surface initially, this would lead to a distortion of the fields in the ϕ direction. Such a geometry cannot be resolved in 2 1/2 D, yet. To include additional geometrical effects that arise from such distortions in the ϕ direction, we need to use a 3 D CME model.

4. The Radiation Model

[15] In a highly structured and temporally evolving plasma like the solar wind, electrons can be energized by shock wave acceleration. If the acceleration is large enough such that the velocity of the accelerated electrons exceeds about two times the thermal velocity of the electrons, the electrons excite Langmuir plasma waves via the beam plasma instability. The solar wind plasma itself is permeated with ion sound waves due to its content of ions. A counterstreaming ion sound wave can annihilate an excited Langmuir wave, which in turn sets free a radio wave at the plasma frequency. Yet, this does not often happen, since the wave number of the ion sound wave is usually much smaller than the wave number of the Langmuir wave. This means that the momentum cannot be conserved in wave number space [see, e.g., *Robinson et al.*, 1993]. In the case that a Langmuir wave is backscattered at an ion sound wave, the reflected wave can annihilate the incoming Langmuir wave. This annihilation process releases a radio wave at the second harmonic plasma frequency.

[16] It is generally believed that shock waves in the heliosphere can significantly increase the first and second harmonic plasma emission in a shock. This is because the large gradients of the fields within a shock generate an additional electric potential field, at which shock drift acceleration of electrons can take place, when the shock

moves out. These highly accelerated electrons in a shock can amplify Langmuir plasma waves due to stochastic growth in the plasma, which in turn can lead to the increased plasma emission.

[17] Using the kinetic analytical theory of shock drift acceleration of electrons and the kinetic analytical theory of stochastic growth of Langmuir waves in a plasma, *Knock et al.* [2001] could successfully reproduce the interplanetary type II event described by *Bale et al.* [1999], with their model for radio type II bursts. In the work of *Knock et al.* [2003] they extended their model to include the geometry of shock ripples. *Knock and Cairns* [2005] investigated the effect of heliospheric structures on radio type II emission. In the study by *Florens et al.* [2007] the *Bale et al.* [1999] event could be simulated in great detail by including a data-driven solar wind model.

[18] In this work we use the kinetic model for a radio type II burst of *Knock et al.* [2001], which is applied to a Maxwell-Boltzmann velocity distribution of upstreaming electrons, to simulate the second harmonic plasma radiation $j_{sh} = j_H$ in CME-driven shock fronts. The data for the CME event are taken from the above MHD model for a CME. This has the purpose to include the full geometry of a CME-driven shock in order to simulate spatially resolved radio images of CMEs observed by radio telescope arrays. How the needed kinetic beam parameters n_b, v_b and Δv_b can be calculated analytically, using the algorithm developed by *Knock et al.* [2001], is specified in the Appendix.

[19] The distinctive features of the kinetic model are as follows: Using the theory of stochastic growth, *Robinson and Cairns* [1998a, 1998b] derived volume emissivities j_M for strongly accelerated electron beams, where $M = F$ for the fundamental plasma radiation and $M = H$ for the second harmonic plasma radiation, that were applied both to radio type III and radio type II bursts. In particular, they found

$$j_M \approx \frac{\Phi_M}{\Delta\Omega_M} \frac{n_b m_e v_b^3}{3l(r)} \frac{\Delta v_b}{v_b}, \qquad (1)$$

where Φ_M is the conversion efficiency of Langmuir waves to radio waves, $\Delta\Omega_M$ is the solid angle over which the emission is spread, i.e., $\Delta\Omega_F = \pi/4$ and $\Delta\Omega_H = 2\pi$, n_b is the beam number density, m_e is the mass of the electron, v_b is the beam velocity, $l(r)$ is the distance along a magnetic field line that links the solar surface with the radio source at heliocentric distance r, and Δv_b is the width of the beam velocity distribution in phase space. Further, it is

$$\Phi_F \approx 72\sqrt{3} \frac{\gamma_{L'}}{\gamma_S} \frac{v_e^3}{c^3} \frac{v_b}{\Delta v_b} \frac{e^{-u_c^2}}{u_c\sqrt{\pi}} \zeta_F, \qquad (2)$$

$$\Phi_H \approx \frac{18\sqrt{3}}{5\gamma_t} \sqrt{\frac{m_i}{\gamma_t m_e}} \frac{v_b^2 v_e^3}{c^5} \frac{v_b}{\Delta v_b} \zeta_H, \qquad (3)$$

where $\gamma_{L'}/\gamma_S$ is the ratio of the damping rates of the product waves in the process $L \rightarrow L' + S$ (L stands for "Langmuir wave", which produces the ion sound wave S that stimulates the fundamental plasma emission), $v_e = (kT_e/m_e)^{1/2}$ is the thermal electron velocity with the Boltzmann constant k

and the electron temperature T_e, u_c represents the fraction of fundamental emission that is able to escape from a source region in which there are significant density irregularities and which has a representative value $u_c = 2.1$, $\gamma_t = 1 + 3 T_i/T_e$, where T_i is the ion temperature, which are protons in our model, m_i is the mass of the ions, and ζ_M are respective fractions of Langmuir waves that are kinematically able to contribute to the fundamental and harmonic emission. It is

$$\zeta_F \approx \exp\left[-\frac{4\gamma_t m_e}{45 m_i}\left(\frac{v_b}{\beta\Delta v_b}\right)^2 \left(\frac{3}{2}\sqrt{\frac{m_i}{\gamma_t m_e}} - \frac{v_b}{v_e}\right)^2\right], \qquad (4)$$

$$\zeta_H \approx \frac{c}{2v_b}\sqrt{\frac{\pi}{6}}\frac{\beta\Delta v_b}{v_b}\left[\text{erf}\left(\frac{\frac{v_e\sqrt{3}}{c} + \frac{2}{3}\sqrt{\frac{\gamma_t m_e}{m_i}}}{\frac{v_e}{v_b}\frac{\beta\Delta v_b}{v_b}\sqrt{2}}\right)\right.$$
$$\left. + \text{erf}\left(\frac{\frac{v_e\sqrt{3}}{c} - \frac{2}{3}\sqrt{\frac{\gamma_t m_e}{m_i}}}{\frac{v_e}{v_b}\frac{\beta\Delta v_b}{v_b}\sqrt{2}}\right)\right], \qquad (5)$$

where $\beta \approx 1/3$ is the width of the model beam-driven Langmuir spectrum, which ensures that this spectrum is negligible outside the range of beam-driven wave vectors. It is important to notice that $\gamma_{L'}/\gamma_S$ is almost zero, if $T_e/T_i \notin \{3\ldots5\}$, i.e., if there are not large temperature anisotropies between electrons and ions. In the case $T_e/T_i \in \{3\ldots5\}$, we get $\gamma_{L'}/\gamma_S \approx \frac{80}{7}\frac{v_e^2}{v_b^2}\sqrt{\frac{mi}{7m_e}}$, and j_F can be of the same order as j_H. Since we do not consider large temperature anisotropies between electrons and ions in our kinetic model, i.e., $T_e/T_i = 1.5$ is assumed within the shock, we can neglect the fundamental plasma radiation that is driven by shock waves in our simulations.

[20] *Knock et al.* [2001] extended this theory of *Robinson and Cairns* [1998a, 1998b] to type II radio emission from a shock. For this purpose, *Knock et al.* [2001] computed the loss cone velocity distribution of the electrons that are reflected at the shock from the velocity distribution of the upstream solar wind electrons: From the reflected loss cone velocity distribution, the required beam parameter n_b, v_b and Δv_b that control the emissivities j_M have been derived numerically. For the ratio $\eta(v_\parallel)$ between the reflected and the upstreaming reduced electron velocity distribution functions, where $v_\parallel$ is the velocity parallel to the magnetic field in the solar wind frame of reference, *Knock et al.* [2001] found

$$\eta(v_\parallel) = 1 - \text{erf}\left[\frac{v_{lc}}{\sqrt{2}\,v_e}\right] + \frac{v_{lc}e^{-v_{lc}^2/2v_e^2}}{\sqrt{\pi/2}\,v_e}, \qquad (6)$$

where v_{lc} is the velocity, up to which the electrons are reflected. It is

$$v_{lc}^2 = \frac{\left(v_\parallel^{HTF}\right)^2 + \frac{2}{m_e}e\Delta\Phi'}{B_2/B_1 - 1}, \qquad (7)$$

where $v_{\parallel}^{HTF} = v_{\parallel} + v_{\parallel}^{WH}$ is the velocity in the Hoffmann-Teller rest frame of the shock, and $v_{\parallel}^{WH} = -v_d \tan \theta_{bn}$ is the relative speed between the solar wind frame and the Hoffmann-Teller frame, $v_d = |-(\mathbf{u} \times \mathbf{B}) \times \mathbf{B}/B^2|$ is the bulk drift velocity of the upstream plasma perpendicular to the magnetic field $\mathbf{B}$ with the upstream velocity $\mathbf{u}$, and θ_{bn} is the angle between the magnetic field and the shock normal, $e\Delta\Phi' \approx 2kT_e (B_2/B_1 - 1)$ with the charge of the electron e is the jump of the electric energy across a collissionless shock due to the additional electric potential in the case that there are no electron temperature anisotropies, and B_2 (B_1) are the magnetic field strength downstream (upstream) the shock with a larger (smaller) value. We can get the reflected loss cone beam electron velocity distribution function in the rest frame of the shock

$$F_r(v_{\parallel r}) = \eta(v_{\parallel})F(v_{\parallel}), \qquad (8)$$

from a given electron velocity distribution function $F(v_{\parallel})$ in the solar wind frame at the location of the shock, if we consider that there is a conservation of the phase space volume along lines in phase space that satisfy

$$v_{\parallel} = -v_{\parallel r} - 2v_{\parallel}^{WH} + u \cos \theta_{ub}, \qquad (9)$$

where θ_{ub} is the angle between the upstream velocity of the electrons and the magnetic field.

[21] *Dulk* [1985] looked at frequency-dependent absorption coefficients and optical depths in the solar corona. He found that the cutoff frequency, above which the fundamental plasma radiation is strongly reabsorbed, is roughly $10-30$ MHz. Even below this limit, the intensity of the fundamental plasma radiation is maximally 1/16 of the intensity of the second harmonic plasma radiation. Since we look at frequencies above 100 MHz in our simulations (164 to 432 MHz are the observing frequencies of the Nançay radioheliograph), we can neglect the component of the fundamental plasma radiation in our simulations. Moreover, the cutoff of the second harmonic plasma radiation due to strong reabsorption happens at frequencies above about $2-5$ GHz. Below that limit, the solar corona is almost optically thin for second harmonic plasma radiation. For this reason no refraction has to be taken into account and no ray tracing techniques are needed to be applied for second harmonic plasma radiation and the construction of synthetic radio maps in the region above about 100 MHz (The refractive index $\bar{n} = \sqrt{1 - \frac{e^2 n_0}{\pi m e f^2}} \approx 1$ for $f \geq 100$ MHz in our simulations).

[22] *Bastian et al.* [2001] observe a CME at frequencies between $164-432$ MHz; the radio emissions are interpreted as synchrotron radiation from nonthermal electron beams. It is the same 20 April 1998 CME as by *Maia et al.* [2000], yet the image by *Bastian et al.* [2001] is taken at a later time at 10:13 UT. *Ramaty and Petrosian* [1972] calculated the effect of self absorption and the Razin effect on gyrosynchrotron emission. They found that the self absorption cutoff frequency is below 5 GHz and the Razin cutoff frequency is

below 2 GHz for gyrosynchrotron radiation in the solar corona (see table 1 in their work). Therefore in the frequency regime of interest, above about 100 MHz, the gyrosynchrotron radiation is almost suppressed. We have neglected the gyrosynchrotron radiation in our simulations for this reason. Bremsstrahlung is the third component of the radio emission of the solar corona [e.g., *Aschwanden*, 2004]. Yet, this thermal (free-free) emission is <1 MK [see, e.g., *Gopalswamy and Kundu*, 1992, 1993]. We have neglected the Bremsstrahlung in our simulations for this reason.

5. Synthetic Radio Maps

[23] In this section we discuss our simulation results based on the CME MHD model and the kinetic radiation model, which we have described in sections 3 and 4.

5.1. Early CME Evolution

[24] Our simulations yield the full information about the spatial distribution of the emission and other physical quantities within the eruption. In Figure 2a we see the field line pattern of the CME in the distorted radial solar field in the x-z plane that is spanned by the in-ecliptic x axis and the rotation axis of the Sun z, both measured in $R_{\odot}$. The field lines are the contour lines of the function $A\phi \, r \sin \theta$, where $A\phi$ is the ϕ-component of the vector potential. The flux rope of the CME is centered in the ecliptic plane. The field lines of the flux rope are spirals that bend in a torus around the z axis. The projections of these field lines on to the x-z plane are circles. These have an anticlockwise sense of rotation in the simulation shown. The magnetic field of the Sun, which is distorted around the flux rope and which becomes almost radial from about 2.5 $R_{\odot}$ heliocentric distance outward, is directed away from the Sun north and south of the CME. We have drawn the magnetic field lines of the Sun as dashed lines in the southern hemisphere, in order to indicate that this magnetic field has the same direction as the magnetic field of the CME in the southern hemisphere. This prohibits magnetic reconnection between them. In the case of antiparallel magnetic fields in the northern and southern hemisphere, there was reconnection of magnetic field lines at the northern and southern edge of the CME, or no reconnection at all. In both cases the CME would evolve symmetrically in the northern and southern hemisphere. The set up of the CME in a unipolar magnetic field chosen here leads to magnetic reconnection at one edge of the CME only. At this edge this reconnection diminishes the magnetic pressure at the boundary of the CME. This has the effect that the CME gets a small momentum in the direction of the reconnection site, and its evolution is not precisely symmetric with respect to the ecliptic plane. Yet, this effect is of minor influence on the radial outward motion of the CME. Magnetic flux conservation requires that there is a directional magnetic field reversal toward the poles of the Sun in this idealized configuration. This field reversal is indicated by the uppermost and lowermost bent field line. The image is taken 2.8 min after the launch of the CME, where the expansion of the CME has led to a squeezing of northern field lines of the CME into the oppositely directed external field lines of the Sun. This has created a reconnection site at the northern edge of the CME, where field lines of the CME are dissolved slowly. The

reconnection in our simulation is due to grid-dependent numerical diffusion. The grid size has been fixed such that the reconnection speed, i.e., the locally induced electric field at the reconnection site normalized to the averaged magnetic field in the vicinity of the reconnection site, is equal to the velocity with which the field lines are pressed together. This means physically that the reconnection is merely due to the Hall effect in our simulations. Such reconnection has been shown to be of significant importance in CME eruptions recently [see, e.g., *Cassak et al.*, 2005, 2006]. At this time, the core of the CME has gone through a rapid acceleration phase, already. It has reached a velocity of about 1200 km s^{-1} in this image, which corresponds to the initial speed of the radio source in the *Maia et al.* [2000] observation.

5.2. Shock

[25] Figure 2b shows a color-coded image of the absolute value of the gradient of the entropy $|\nabla(p/\rho^\gamma)|$, where p is the solar wind pressure, ρ is the solar wind mass density and the gradient is calculated with finite differences on the numerical grid. We use this image for tracing the shock wave. Thus we only need to notice that cold colors like blue belong to small values of the displayed variable, whereas warm colors like red belong to large values of the displayed variable in this image. The boundaries of shock waves can be determined quite precisely by looking at jumps in the entropy of the system. At the steep front of the shock, the gradient of the entropy jumps from a greenish value to black almost sharply. There is an outward front of the CME-driven shock. This front is moving away from the CME and it is the outermost almost circular boundary of the green ring in the image. We can also trace the CME-driven shock in the field line image of Figure 2a, where there is an enhanced number density of field lines at the location of the shock wave. (This feature can be seen more prominently in Figures 3a and 4a, where the shock has developed further.) Thus the CME-driven shock wave is an area of enhanced downstream magnetic field strength, too.

[26] Secondly, there is a weak inward shock front of the CME-driven shock wave. This shock front is still moving away from the CME and it is the innermost almost circular boundary of the greenish ring in the image. Obviously, the occurrence of this second shock front is a consequence of the 2 1/2 D geometry. In this geometry, the inner cylindrical volume of the flux rope extends in the ϕ direction indefinitely. A sudden release of a pressure pulse within such an initial flux rope geometry of the CME produces a forward and a reverse shock. The latter can develop, since there are no constraints of the volume in the ϕ direction. Yet, we find that this initial weak inward shock front has little influence on our radiation simulation results.

[27] The large absolute values of the gradient of the entropy of the CME-driven shock wave between the outermost and the innermost boundaries of this greenish ring area reveal that the content of thermal energy within the CME-driven shock wave is huge due to the compression of the plasma. There is another area with heated plasma, which is the bluish almost circular area in the middle of the ring. Obviously, overpressured core plasma within a torus that occupies about 80 percent of the original flux rope geometry is still trying to push plasma away from the core region of the CME. Yet, the tension forces within the closed spiral field lines of the flux rope of the CME prohibit a free relaxation of this core plasma, thus keeping a high plasma temperature.

5.3. Emissivity

[28] Figure 2c shows the color-coded volume emissivity of the second harmonic plasma radiation $j_{sh}(2\omega_p)$, where ω_p is the local plasma frequency. The color bar indicates the value of the volume emissivity. The shock region in this plot, which is of the same almost circular shape and at the same location as the front part of the ring-shaped shock region in Figure 2b, emits predominantly with about 5×10^{-22} W m^{-3} sr^{-1}, with peak emissivities reaching up to 1×10^{-17} W m^{-3} sr^{-1}. This range of volume emissivities falls within the range of those measured for interplanetary type II bursts ($\approx 10^{-18}$ W m^{-3} sr^{-1} around the drifting line of the type II burst in the radiogram of *Bale et al.* [1999]) and those simulated for interplanetary type II bursts ($\approx 10^{-21}$ W m^{-3} sr^{-1} on average in the simulations of *Knock et al.* [2001] for the same event). Within this ring segment of the shock, we find a spatially structured enhancement of the emission. This enhancement is just behind the front of the shock and has a shell shape, where the emission increases to about 1×10^{-17} W m^{-3} sr^{-1} toward the center point of the shell. This enhancement is mainly due to the large gradient of the magnetic field in the vicinity of the front of the shock that makes shock drift acceleration of electrons and stochastic growth of Langmuir waves most effective at and behind the front of the shock (also compare with the radiation formulae, where a growing ratio B_2/B_1 of the downstream over upstream magnetic field enhances the radiation).

5.4. Emission Frequency

[29] It is important to realize that a telescope that receives at a fixed frequency cannot detect a radio image like in Figure 2c exactly. In the whole field of view between one and four $R_\odot$ the plasma density decreases with distance as well as disturbed by the CME. This has the effect that the emission frequency, which is twice the plasma frequency, has different values at different points. Figure 2d displays the color-coded emission frequency distribution in our simulation. To the right of Figure 2d, a color bar shows which emission frequency belongs to which color. If we tuned our telescope to about 295 MHz, plus or minus a telescope-specific bandwidth of received frequencies in the order of 35 MHz, radio sources that occur in the area of Figure 2d that emits at about 260 MHz would be visible. Since this area that emits at about 260 MHz includes a sharp ring region from the northern via the eastern to the southern part of the shock region in Figure 2c, we would detect the shock as an elongated banana-shaped radio source at that frequency, which is populated around the inner edge of the shock.

[30] There is a density increase in the center of the CME and a pile up of density at the rear of the CME. Both increases lead to an increased emission frequency of about 554 MHz in the center and at the rear part of the CME in Figure 2d. Yet, in these regions of the CME there is no emissivity.

[31] These features compare well to the *Maia et al.* [2000] Nançay radioheliograph observation at 327 MHz of the 20 April 1998 CME-event at 9:43 UT. There, the CME-driven shock was first seen as a bent radio source.

5.5. CME at Intermediate State

[32] Figure 3 shows the state of the CME eruption after 25.4 min real time have elapsed. Since there is a sharp jump of the absolute value of the entropy gradient from violet to black in Figure 3b of that image, the CME-driven shock has developed fully. Also, the maximum heliocentric distance of the shock front reached is almost 2.9 $R_\odot$. This shock front almost encircles the CME in the r-θ plane. Since the shock front is along a circle in the ϕ direction, also, the entire three-dimensional shock is almost situated on a section of a sphere. This might be the explanation for the observational fact that many halo CMEs are seen as an almost spherical structure in coronagraph images. Figure 3a with the magnetic field line pattern reveals that the area of shocked plasma around the CME has field lines with increased number density. The core of the CME has been accelerated further, and it has reached a velocity of about 1300 km s^{-1} at this stage. As in Figure 2, the shock front defines the border line of an area that has an increased volume emissivity from about 5×10^{-25} W m^{-3} sr^{-1} to about 1×10^{-17} W m^{-3} sr^{-1} in Figure 3c. The emission drops very sharply from about 1×10^{-17} W m^{-3} sr^{-1} to about 5×10^{-28} W m^{-3} sr^{-1} at the front part of the shock. We can see in the field line pattern in Figure 3a that the field lines of the distorted radial magnetic field of the Sun have the largest bend at the front part of the shock. This makes that front to an almost perpendicular shock front. Since quasi-perpendicular shocks are the most effective particle accelerators, this might explain the highly increased emission at the front part of the shock. Figure 3d shows that the front part of the shock with a specific width emits at an emission frequency of about 231 MHz. If we look from the front of the shock closer to the center of the CME, there is a steep decrease in the emission frequency to an almost zero value. This is caused by the rarefaction of the density in the center of the CME due to the over expansion of the CME. The effect of this is that a telescope, tuned to about 231 MHz, would see an eclipse of the radio signal toward the center of the CME. This is because the emission frequency slips out of the range 231 MHz plus or minus a specific bandwidth of the receiver. Thus the telescope would see the radio source as a banana-shaped feature along the inside of the shock front of the CME. Toward the northern and southern edge of this elongated radio source, the area that emits at about 231 MHz in the frequency distribution plot extends into regions with decreasing emissivity. The result of this is that there is an eclipse of the radio signal at the northern and southern edge of the CME-driven shock for a telescope that observes with a fixed frequency, too.

[33] These features correspond to the *Maia et al.* [2000] Nançay radioheliograph observation at 236 MHz of the 20 April 1998 CME event at 9:45 UT. There, a bent banana-shaped radio source was seen with a location on top of an area with an increasingly faint radio signal, if we look closer to the Sun.

5.6. CME Close to 4 $R_\odot$

[34] In Figure 4 we see the state of the CME after 47.7 min real time have elapsed. The CME has been accelerated further to about 1400 km s^{-1}, and the shock front of the CME has reached a heliocentric distance of about 3.7 $R_\odot$. We see that the shock has grown in diameter considerably. Yet, it has maintained its almost circular shape around the CME in the r-θ plane.

[35] The frequency distribution in Figure 4d reveals that the region behind the shock wave emits at about 130 MHz. Again, a telescope that was tuned to about 130 MHz plus or minus a specific bandwidth of the receiver would see this region as an elongated radio source with banana-like shape along the boundary of the shock. This is due to the decrease of the emission frequency toward the center of the CME, where the density decreases significantly and the emission frequency slips out of the detectable range.

[36] These features correspond to the *Maia et al.* [2000] Nançay radioheliograph observation at 164 MHz of the 20 April 1998 CME event after 9:50 UT. We see a quite distinct banana-shaped radio source that surrounds the CME's leading edge and moves outward with almost the same emission frequency.

5.7. Synthetic Radio Type II Burst

[37] Figure 5 shows the synthetic radio type II burst of our simulation, which consists of a decreasing line of emissivity enhancements in a frequency over time diagram. This image is constructed as follows. At each specific time in the simulation, the emission frequency of each of the 30,000 cells in the simulation box is determined. About 1500 of these cells are within the shock. Each of such pairs of time and frequency values defines a specific point in the time-frequency diagram, which has a sum value of volume emissivities assigned. To this sum value, the volume emissivities of the cells that emit at this specific frequency and at this specific time are added, and this process is repeated for all cells and over all times. Then, a numerical filter that mimics the sensitivity curve of a receiver is applied to the image. This numerical filter consists of a Gaussian function with a width of about the range of emissivities found in our simulation. This filter has the effect that drifting lines of emission enhancements become much sharper in the frequency-time diagram. Since the number of cells is restricted, the resolution of the image is also restricted. Values of the emissivity are indicated by the color bar at the right of the image.

[38] There is a curved line of emission enhancement with an almost hyperbolic shape in that image, which emits at about 5×10^{-22} W m^{-3} sr^{-1} to 1×10^{-17} W m^{-3} sr^{-1} (see labels "1" in Figure 5). This line constitutes the synthetic radio type II burst [see, e.g., *Florens et al.*, 2007, for an example of an observed interplanetary radio type II burst that has this hyperbolic shape]. The steeper branch of that hyperbolic curve reaches from about 315 MHz at about 5.5 min to about 160 MHz at about 6 min in our image (see label "2" in Figure 5). It is followed by a knee-shaped part of the curve that ends at about 100 MHz at about 20 min (see label "3" in Figure 5). The hyperbolic curve continues with a flatter branch that extends to about 70 MHz at about 44 min (see label "4" in Figure 5). The curve is diffusive as the peak emission is not localized. Scattered signals outside
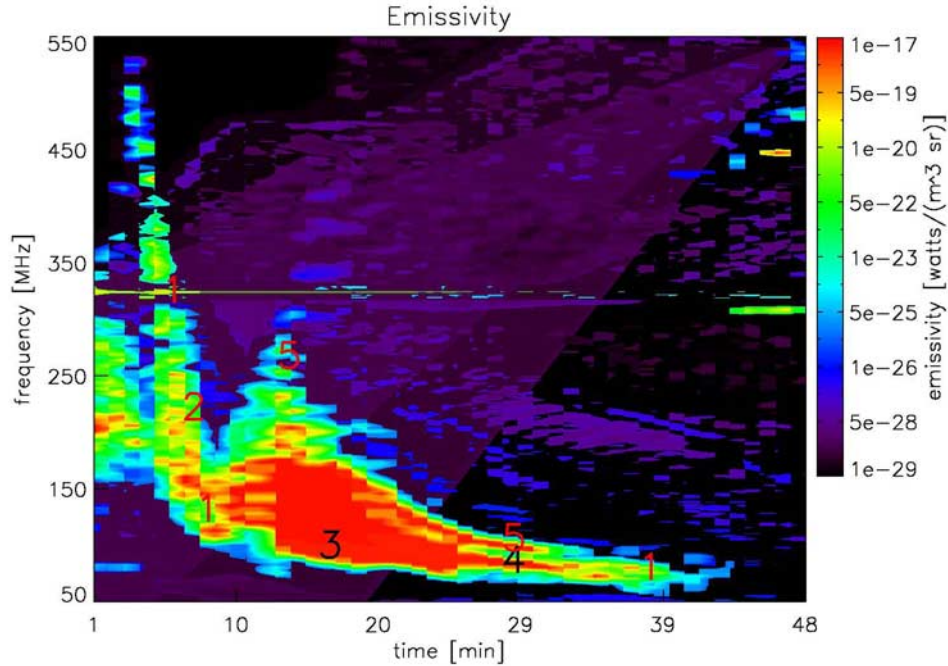
Figure 5. Simulated radio type II burst, which consists of an almost hyperbolic line of emission enhancement in the frequency-time diagram with emissions from about 5×10^{-22} W m^{-3} sr^{-1} to 1×10^{-17} W m^{-3} sr^{-1} that has a steeper branch from ~315 MHz at about 5.5 min to ~160 MHz at about 6 min (label "2"), a knee that reaches to ~100 MHz at about 20 min (label "3"), and a flatter branch that extends to ~70 MHz at about 44 min (label "4"). A second hyperbolic curve is present from ~280 MHz at 13 min to ~90 MHz at 31 min (labels "5"). It is a consequence of the complex density structure within the shock.

this curve or at about 5×10^{-28} W m^{-3} sr^{-1} are from all kinds of density disturbances throughout the CME eruption that cause a jump in the emission frequency. The center of this hyperbolic curve must not necessarily coincide with the frequency at which the CME-driven shock front emits, when the majority of the emission is in regions of the CME outside the shock. There is a second hyperbolic curve in the image (see labels "5" in Figure 5). This second curve starts at about 280 MHz at 13 min. It continues from about 160 MHz to 90 MHz between about 16 min and 31 min as a parallel curve above the first hyperbolic curve. This splitting of curves into upper and lower bands in drifting radio type II bursts, thought to be caused by the density structure in the shock [see, e.g., *Nelson and Melrose*, 1985; *Vrsnak et al.*, 2001], has been reported, e.g., by *Cane and Erickson* [2005] (see Figure 1 in this work), who combined Culgoora, Bruny Island Radio Spectrometer (BIRS) and WAVES/WIND radio emission data to trace radio type II bursts from 570 MHz to 20 kHz.

5.8. Acceleration History of CME

[39] Figure 6 shows the height $h(t)$ (in $R_\odot$), the velocity $v(t)$ (in 10^3 km/s), and the acceleration $a(t)$ (in km/s^2) of the shock. $v(t)$ and $a(t)$ are calculated with finite differences from the grid points where $h(t)$ is available. Since there are only a few of such grid points, we get some numerical error for $h(t)$, $v(t)$ and $a(t)$. This explains why the curves are not

very smooth, and the numerical error is larger for $v(t)$ and the largest for $a(t)$. The shock starts at about 1.75 $R_\odot$ heliocentric distance, which is forced to be consistent with the *Maia et al.* [2000] observations. In the beginning, the shock experiences a considerable acceleration, reaching a peak velocity of about 1800 km/s after about 5 min. Then, the shock is decelerated. This can be detected in the slight right bend of the curve $h(t)$ and the decreasing branch of $v(t)$ between about 5 and 18 min. Also $a(t)$ is negative in this time interval and has largest negative values of about -1.5 km/s^2 between about 6 and 11 min. At about 18 min, the shock reaches a minimum velocity of about 900 km/s. Then, the shock is outward accelerated again and it has a second maximum of the velocity of about 1200 km/s at about 25 min. Another deceleration phase of the shock with negative $a(t)$ follows up to about 33 min, where the shock reaches a velocity of about 900 km/s again. After that point, the shock is outward accelerated continuously, and it reaches a velocity of about 1400 km/s at the end of the simulation. This is consistent with the *Maia et al.* [2000] observations, too. A possible explanation for this oscillative acceleration history of the shock is that the shock-driving CME is over-expanding in the beginning. When the CME grows in size the magnetic buoyancy force on the CME becomes more effective. This increases the outward acceleration of the CME. When the CME moves (due to increased outward acceleration) into regions with decreased
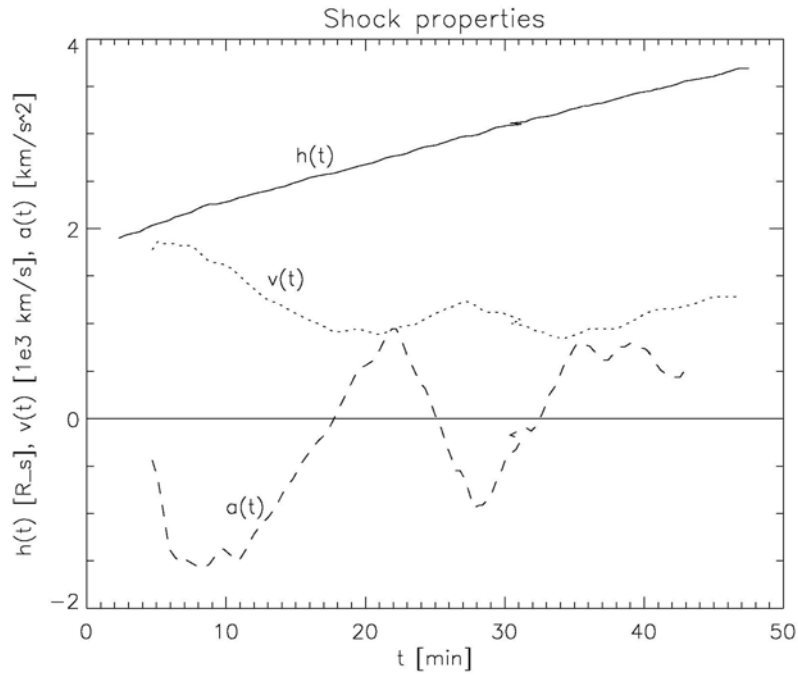
Figure 6. Height of the shock $h(t)$ above the Sun's center, the shock's velocity $v(t)$ and the shock's acceleration $a(t)$. The height of the shock increases continuously. Yet, the shock experiences slight oscillations in its velocity. These might be the consequence of a shock-driving CME that is subject to increased magnetic buoyancy, counteracting the gravitational force of the Sun and retarding drag forces of the solar wind, when it is over-expanding and subject to decreased magnetic buoyancy forces when it moves into regions of decreased magnetic field strength within a radially diverging magnetic field of the Sun.

magnetic field strength in the diverging magnetic field of the Sun, the acceleration due to magnetic buoyancy forces decreases. Eventually, the sum of the gravitational force and the retarding drag force of the solar wind on the CME becomes relatively larger than the magnetic buoyancy force, and the CME is decelerated. Then, a continuous growth of the CME due to further over expansion makes the magnetic buoyancy force on the CME more effective again. It finally compensates and outnumbers the sum of the gravitational force and the drag force, relatively. Then, the CME starts being outward accelerated again. This process of successive acceleration and deceleration in a system of disturbed balance between magnetic buoyancy, drag and gravitation can be repeated. A discussion of the three forces acting on a smaller plasmoid in the solar atmosphere can be found, e.g., by *Schmidt and Cargill* [2000]. Note that due to time intervals with significant low velocities the CME reaches smaller heliocentric distances than as if it would propagate with the observed average speed 1400 km/s for all the time.

5.9. Fit Parameter for Radio Type II Burst

[40] Ideally, for the frequency we have

$$2\pi f = 2\omega_p = 2\left(\frac{n_0 e^2}{\epsilon_0 m_e}\right)^{1/2}, \tag{10}$$

where the plasma electron number density n_0 roughly follows a $1/r^2$-law due to the spherical expansion of the solar wind. ϵ_0 is the permittivity of free space.

$$\Rightarrow\ f \approx \frac{1}{\pi}\sqrt{\frac{e^2}{\epsilon_0 m_e}\frac{n_0(r_0)}{\left(\frac{r}{r_0}\right)^2}}, \tag{11}$$

where r_0 is the heliocentric distance at which the shock starts. Further, we have

$$r \approx r_0 + \langle v_{source}\rangle t, \tag{12}$$

where $\langle v_{source}\rangle$ is the averaged velocity of the outward propagating shock.

$$\Rightarrow\ f \approx \frac{\bar{\alpha}}{1 + \bar{\beta}t} = y(t), \tag{13}$$

where $\bar{\alpha} = \frac{1}{\pi}\sqrt{\frac{e^2 n_0(r_0)}{\epsilon_0 m_e}}$ and $\bar{\beta} = \frac{\langle v_{source}\rangle}{r_0}$. On the curve $f = y(t)$ we have N data points (t_i, f_i). These are gained from Figure 5 as follows: At each temporal cut t_i in the simulation we take f_i as the mid point of the lower hyperbolic curve with some width in that figure. Then, these pairs can be used to find the best fitting parameters $\bar{\alpha}$ and $\bar{\beta}$ in a nonlinear least squares fit. Obviously, there is a strong acceleration phase followed by a deceleration phase of the CME for $t < 5$ min. If we take all data points on the curve for $t \geq 5$ min in our simulation,

we get $\bar{\bar{\beta}} = 0.00129979$ s^{-1} and $\bar{\alpha} = 2.89625 \times 10^8$ s^{-1}. Since $r_0 = 1.685\ R_\odot$ in our simulations,

$$\langle v_{source}\rangle = \bar{\beta}r_0 = 1{,}524\ \text{km/s}.$$

[41] This is about the average speed of the shock in our simulations and also about the averaged observed shock speed. For the plasma number density estimate we get

$$n_0(r_0) \approx \epsilon_0 m_e \left(\frac{\pi\bar{\alpha}}{e}\right)^2 = 2.60 \times 10^8\ \text{cm}^{-3}.$$

[42] This is a value slightly below the inner boundary value $n_0(R_\odot) = 3.3 \times 10^8$ cm^{-3} in our simulations. Our results compare with the results obtained by *Knock et al.* [2001], who simulated the radio type II burst observed by *Bale et al.* [1999], where the average shock speed is 1300 km/s, the local Alfvén speed is 5.7×10^4 m s^{-1}, $B_1 = 7$ nT, $B_2/B_1 = 3$, and the compression ratio is 3.7 (all values taken at 1 AU), if we interpolate the corresponding number density of $\approx$239 cm^{-3} in the shock at 1 AU back to 1.685 $R_\odot$ with a Parker density profile.

[43] These precise fits for shock speeds and number densities in our computations for frequency drifts show that we can simulate radio type II bursts successfully.

6. Conclusions

[44] Our simulations of a CME eruption and its excited radio emission in a region beneath about four $R_\odot$ heliocentric distance have shown that the initial release of an overpressured flux rope creates a shock wave that surrounds the CME and which is an effective radio emitter. The steepening of the shock during the shock evolution creates a large gradient of the magnetic field. This gradient corresponds to an electron beam driving acceleration potential that can enhance the radio emission in the shock significantly. Thus the shock front appears as a very sharp border line of the radio emitting area in our simulations. The shock spreads rapidly and reaches an almost spherical shape at the end of the simulation.

[45] The CME over expands due to the initial over pressure within the CME. This creates a rarefaction region in the center of the CME. This has the effect that the double plasma frequency decreases, if we look from the shock toward the center of the CME. A fixed-frequency receiver would sense an eclipse of the radio signal toward the center of the CME, where the frequency of the signal slips out of the detectable range of the center frequency. Thus the telescope, like the Nançay radioheliograph, would see banana-shaped radio sources along the leading edge of the CME.

[46] LOFAR, which becomes operational in 2009 and reaches spatial resolutions below one arc second, and whose receiving frequency can be tuned, will be able to resolve the spatial structures that are seen in our synthetic radio maps of a CME. Therefore our simulations can help with the interpretation of future LOFAR observations and other spatially resolved radio telescope observations of CMEs below four $R_\odot$ heliocentric distance.

[47] We are able to simulate the temporal and spatial behavior of radio type II bursts.

Appendix A: Reflected Electron Beam Parameters

[48] In this work we use a Maxwell-Boltzmann velocity distribution function

$$F(v_\parallel) = 4\pi \left(\frac{m_e}{2\pi kT_e}\right)^{3/2} v_\parallel^2 \exp\left(-\frac{m_e v_\parallel^2}{2kT_e}\right) \tag{A1}$$

for the velocity distribution of the electrons upstream of the shock. By substituting (9) and using (8), we get

$$n_b = \int_0^\infty F_r(v_{\parallel r}) dv_{\parallel r}, \tag{A2}$$

$$v_b = \int_0^\infty v_{\parallel r} F_r(v_{\parallel r}) dv_{\parallel r}, \tag{A3}$$

$$\langle v_{\parallel r}^2\rangle = \int_0^\infty v_{\parallel r}^2 F_r(v_{\parallel r}) dv_{\parallel r}, \tag{A4}$$
$$\Delta v_b = \sqrt{\langle v_{\parallel r}^2\rangle - v_b^2}.$$

[49] These integrals can be solved approximately, by choosing $x = \sqrt{(B_2/B_1 - 1)v_{lc}^2 - \frac{2}{m_e}e\Delta\Phi'}$ as the new integration variable, considering that we have $v_{lc} \approx x/\sqrt{B_2/B_1 - 1}$ in a very good approximation, which makes the integrands to rational functions in x times a Maxwellian in x, substituting again with $\tilde{x} = x - A$, where A is taken from (A11), and approximating $\tilde{x} + A \approx \tilde{x}$, where $\tilde{x}$ is much larger than A, in the one place where this sum occurs in the denominator of the integrands, which makes the integrands to polynomials in $\tilde{x}$ times a Maxwellian in $\tilde{x}$. These integrals can be processed further, if we consider that for positive integer numbers n we have

$$\int_B^\infty \tilde{x}^{2n+1} e^{-\alpha\tilde{x}^2} d\tilde{x} = \frac{1}{2}\int_{B^2}^\infty \tilde{\tilde{x}}^n e^{-\alpha\tilde{\tilde{x}}} d\tilde{\tilde{x}}, \quad \text{where } \tilde{\tilde{x}} = \tilde{x}^2$$

$$= \frac{1}{2}\frac{d^n}{d(-\alpha)^n}\int_{B^2}^\infty e^{-\alpha\tilde{\tilde{x}}} d\tilde{\tilde{x}}$$

$$= \frac{(-1)^n}{2}\frac{d^n}{d\alpha^n}\frac{e^{-\alpha B^2}}{\alpha}, \tag{A5}$$

$$\int\limits_B^\infty \tilde{x}^{2n} e^{-\alpha \tilde{x}^2} d\tilde{x} = \frac{d^n}{d(-\alpha)^n} \int\limits_B^\infty e^{-\alpha \tilde{x}^2} d\tilde{x}$$

$$= \frac{(-1)^n}{2} \frac{d^n}{d\alpha^n} \frac{1}{\sqrt{\alpha}} 2 \int\limits_{\sqrt{\alpha} B}^\infty e^{-t^2} dt,$$

where $t = \sqrt{\alpha}\, \tilde{x}$

$$\approx \frac{(-1)^n}{2} \frac{d^n}{d\alpha^n} \frac{e^{-\alpha B^2}}{\alpha B}, \tag{A6}$$

where we used the approximation $2\int\limits_y^\infty e^{-t2}\, dt \approx \frac{e^{-y2}}{y}$. With the formulae (A5) and (A6) the necessary integrations can be reduced to differentiation tasks. Putting all terms together, the result of this tedious calculation is

$$n_b \approx \frac{2}{\pi} \frac{1}{v_e^3} \exp\left(-\frac{A^2}{2v_e^2(B_2/B_1)}\right) e^{-B^2} X$$
$$\cdot \left[\left(\frac{B^2+1}{2} X^3 + \frac{(B_2/B_1 - 3)A}{B_2/B_1} \frac{B^2+1}{2B} X^2 \right.\right.$$
$$\left.+ \frac{A^2(3-2B_2/B_1)}{2(B_2/B_1)^2} X + \frac{A^3(B_2/B_1 - 1)}{2(B_2/B_1)^3 B} \right)$$
$$\times \frac{1}{v_e \sqrt{B_2/B_1 - 1}} + v_e \sqrt{B_2/B_1 - 1}$$
$$\left.\times \left(\frac{1}{2} X - \frac{A}{2B B_2/B_1} \right) \right], \tag{A7}$$

$$v_b \approx \frac{2}{\pi} \frac{1}{v_e^3} \exp\left(-\frac{A^2}{2v_e^2(B_2/B_1)}\right) e^{-B^2} X$$
$$\cdot \left[\left(\frac{B^4 + 2B^2 + 2}{2B} X^4 + \frac{(B_2/B_1 - 3)A}{B_2/B_1} \frac{B^2+1}{2} X^3 \right.\right.$$
$$\left.+ \frac{A^2(3-2B_2/B_1)}{(B_2/B_1)^2} \frac{B^2+1}{2B} X^2 + \frac{A^3(B_2/B_1 - 1)}{2(B_2/B_1)^3} X \right)$$
$$\times \frac{1}{v_e \sqrt{B_2/B_1 - 1}} + v_e \sqrt{B_2/B_1 - 1}$$
$$\times \left(\frac{B^2+1}{2B} X^2 - \frac{A}{2B_2/B_1} X \right)$$
$$+ \left(\frac{B^2+1}{2} X^3 + \frac{(B_2/B_1 - 3)A}{B_2/B_1} \frac{B^2+1}{2B} X^2 \right.$$
$$\left.+ \frac{A^2(3-2B_2/B_1)}{2(B_2/B_1)^2} X + \frac{A^3(B_2/B_1 - 1)}{2B(B_2/B_1)^3} \right)$$
$$\times \frac{C}{v_e \sqrt{B_2/B_1 - 1}} + v_e \sqrt{B_2/B_1 - 1}\, C$$
$$\left.\times \left(\frac{1}{2} X - \frac{A}{2B B_2/B_1} \right) \right], \tag{A8}$$

$$\langle v_{\|r}^2 \rangle \approx \frac{2}{\pi} \frac{1}{v_e^3} \exp\left(-\frac{A^2}{2v_e^2(B_2/B_1)}\right) e^{-B^2} X \left[\left(\frac{B^4 + 2B^2 + 2}{2} X^5 \right.\right.$$
$$+ \frac{(B_2/B_1 - 3)A}{B_2/B_1} \frac{B^4 + 2B^2 + 2}{2B} X^4$$
$$\left.+ \frac{A^2(3-2B_2/B_1)}{(B_2/B_1)^2} \frac{B^2+1}{2} X^3 + \frac{A^3(B_2/B_1 - 1)}{(B_2/B_1)^3} \frac{B^2+1}{2B} X^2 \right)$$
$$\times \frac{1}{v_e \sqrt{B_2/B_1 - 1}} + v_e \sqrt{B_2/B_1 - 1}$$
$$\cdot \left(\frac{B^2+1}{2} X^3 - \frac{A}{B_2/B_1} \frac{B^2+1}{2B} X^2 \right)$$
$$+ \left(\frac{B^4 + 2B^2 + 2}{2B} X^4 \right.$$
$$+ \frac{(B_2/B_1 - 3)A}{B_2/B_1} \frac{B^2+1}{2} X^3$$
$$\left.+ \frac{A^2(3-2B_2/B_1)}{(B_2/B_1)^2} \frac{B^2+1}{2B} X^2 + \frac{A^3(B_2/B_1 - 1)}{2(B_2/B_1)^3} X \right)$$
$$\times \frac{2C}{v_e \sqrt{B_2/B_1 - 1}} + v_e \sqrt{B_2/B_1 - 1}\, 2C$$
$$\times \left(\frac{B^2+1}{2B} X^2 - \frac{A}{2B_2/B_1} X \right)$$
$$+ \left(\frac{B^2+1}{2} X^3 + \frac{(B_2/B_1 - 3)A}{B_2/B_1} \frac{B^2+1}{2B} X^2 \right.$$
$$\left.+ \frac{A^2(3-2B_2/B_1)}{2(B_2/B_1)^2} X + \frac{A^3(B_2/B_1 - 1)}{(B_2/B_1)^3 2B} \right)$$
$$\times \frac{C^2}{v_e \sqrt{B_2/B_1 - 1}} + v_e \sqrt{B_2/B_1 - 1}\, C^2$$
$$\left.\times \left(\frac{1}{2} X - \frac{A}{2B B_2/B_1} \right) \right], \tag{A9}$$

where

$$X = \frac{\sqrt{2v_e^2(B_2/B_1 - 1)}}{\sqrt{B_2/B_1}}, \tag{A10}$$

$$A = v_d \tan\theta_{bn} + u \cos\theta_{ub}, \tag{A11}$$

$$B = \frac{\sqrt{B_2/B_1}(-v_d \tan\theta_{bn} - A) + \frac{A}{\sqrt{B_2/B_1}}}{\sqrt{2v_e^2(B_2/B_1 - 1)}}, \tag{A12}$$

$$C = -\frac{A}{B_2/B_1} + (v_d \tan\theta_{bn} + A). \tag{A13}$$

References

Aschwanden, M. (2004), *Physics of the Solar Corona*, Springer, New York.

Aschwanden, M. J., S. J. Newmark, J.-P. Delaboudinière, W. M. Neupert, J. A. Klimchuk, G. A. Gary, F. Portier-Fozzani, and A. Zucker (1999), Three-dimensional stereoscopic analysis of solar active region loops. part I: SOHO/EIT observations and temperatures of $(1.0-1.5) \times 10^6$ K, *Astrophys. J.*, 515, 842–867, doi:10.1086/307036.

Bale, S. D., M. J. Reiner, J. L. Bougeret, M. L. Kaiser, S. Krucker, D. E. Larson, and R. P. Lin (1999), The source region of an interplanetary type II radio burst, *Geophys. Res. Lett.*, 26, 1573–1576.

Bastian, T. S., M. Pick, A. Kerdraon, D. Maia, and A. Vourlidas (2001), The coronal mass ejection of 1998 April 20: Direct imaging at radio wavelengths, *Astrophys. J.*, 558, L65–L69.

Bougeret, J.-L., et al. (1995), Waves: The radio and plasma wave investigation on the Wind spacecraft, *Space Sci. Rev.*, 71, 231–263.

Brueckner, G. E., et al. (1995), The Large Angle Spectroscopic Coronagraph (LASCO), *Sol. Phys.*, 162, 357–402.

Cane, H. V., and W. C. Erickson (2005), Solar type II radio bursts and IP type II events, *Astrophys. J.*, 623, 1180–1194, doi:10.1086/428820.

Cane, H. V., N. R. Sheeley, and R. A. Howard (1987), Energetic interplanetary shocks, radio emission, and coronal mass ejections, *J. Geophys. Res.*, 92, 9869–9874.

Cargill, P. J., J. M. Schmidt, D. S. Spicer, and S. T. Zalesak (2000), Magnetic structure of overexpanding coronal mass ejections: Numerical models, *J. Geophys. Res.*, 105, 7509–7520.

Cassak, P. A., M. A. Shay, and J. F. Drake (2005), Catastrophe model for fast magnetic reconnection onset, *Phys. Rev. Lett.*, 95, 235 002, doi:10.1103/PhysRevLett.95.235002.

Cassak, P. A., J. F. Drake, and M. A. Shay (2006), A model for spontaneous onset of fast magnetic reconnection, *Astrophys. J.*, 644, L145–L148, doi:10.1086/505690.

Cremades, H., and V. Bothmer (2004), On the three-dimensional configuration of coronal mass ejections, *Astron. Astrophys.*, 422, 307–322.

Crooker, N., J. A. Joselyn, and J. Feynman (1997), *Coronal Mass Ejections*, AGU, Washington, D. C.

DeVore, C. R. (1991), Flux-corrected transport techniques for multidimensional compressible MHD, *J. Comput. Phys.*, 92, 142–160.

Dulk, G. A. (1985), Radio emission from the sun and stars, *Annu. Rev. Astron. Astrophys.*, 23, 169–224.

Florens, M. S. L., I. H. Cairns, S. A. Knock, and P. A. Robinson (2007), Data-driven solar wind model and prediction of type II bursts, *Geophys. Res. Lett.*, 34, L04104, doi:10.1029/2006GL028522.

Forbes, T. G., et al. (2006), CME theory and models, *Space Sci. Rev.*, 123, 251–302, doi:10.1007/s11214-006-9019-8.

Gopalswamy, N. (2006), Coronal mass ejections of solar cycle 23, *J. Air Waste Manage. Assoc.*, 27, 243–254.

Gopalswamy, N., and M. R. Kundu (1992), Estimation of the mass of a coronal mass ejection from radio observations, *Astrophys. J.*, 390, L37–L39.

Gopalswamy, N., and M. R. Kundu (1993), Thermal and nonthermal emission during a coronal mass ejection, *Sol. Phys.*, 143, 327–343.

Gopalswamy, N., A. Lara, R. P. Lepping, M. L. Kaiser, D. Berdichevsky, and O. C. St. Cyr (2000), Interplanetary acceleration of coronal mass ejections, *Geophys. Res. Lett.*, 27, 145–148.

Gopalswamy, N., E. Aguilar-Rodriguez, S. Yashiro, S. Nunes, M. L. Kaiser, and R. A. Howard (2005), Type II radio bursts and energetic solar eruptions, *J. Geophys. Res.*, 110, A12S07, doi:10.1029/2005JA011158.

Gosling, J. T., P. Riley, D. J. McComas, and V. J. Pizzo (1998), Overexpanding coronal mass ejections at high heliographic latitudes: Observations and simulations, *J. Geophys. Res.*, 103, 1941–1954.

Hundhausen, A. J. (1999), Coronal mass ejections, in *The Many Faces of the Sun: A Summary of the Results From NASA's Solar Maximum Mission*, edited by K. T. Strong et al., 143 pp., Springer, New York.

Hundhausen, A. J., C. B. Sawyer, L. L. House, R. M. E. Illing, and W. J. Wagner (1984), Coronal mass ejections observed during the Solar Maximum Mission: Latitude distribution and rate of occurrence, *J. Geophys. Res.*, 89, 2639–2646.

Klein, L. W., and L. F. Burlaga (1982), Interplanetary magnetic clouds at 1 AU, *J. Geophys. Res.*, 87, 613–624.

Knock, S. A., and I. H. Cairns (2005), Type II radio emission predictions: Sources of coronal and interplanetary spectral structure, *J. Geophys. Res.*, 110, A01101, doi:10.1029/2004JA010452.

Knock, S. A., I. H. Cairns, P. A. Robinson, and Z. Kuncic (2001), Theory of type II radio emission from the foreshock of an interplanetary shock, *J. Geophys. Res.*, 106, 25,041–25,051.

Knock, S. A., I. H. Cairns, and P. A. Robinson (2003), Type II radio emission predictions: Multiple shock ripples and dynamic spectra, *J. Geophys. Res.*, 108(A10), 1361, doi:10.1029/2003JA009960.

Maia, D., M. Pick, A. Vourlidas, and R. Howard (2000), Development of coronal mass ejections: Radio shock signatures, *Astrophys. J.*, 528, L49–L51.

Nelson, G. J., and D. B. Melrose (1985), Type II bursts, in *Solar Radiophysics: Studies of Emission From the Sun at Metre Wavelengths*, edited by D. McLean and N. Labrum, pp. 333–359, Cambridge Univ. Press, New York.

Pneuman, G. W. (1984), The "melon-seed" mechanism and coronal transients, *Sol. Phys.*, 94, 387–411.

Ramaty, R., and V. Petrosian (1972), Free-free absorption of gyro-synchrotron radiation in solar microwave bursts, *Astrophys. J.*, 178, 214–249.

Reiner, M. J., M. L. Kaiser, J. Fainberg, and R. G. Stone (1998), A new method for studying remote type II radio emissions from coronal mass ejection-driven shocks, *J. Geophys. Res.*, 103, 29,651–29,664.

Robinson, P. A., and I. H. Cairns (1998a), Fundamental and harmonic emission in type III solar radio bursts. part I: Emission at a single location or frequency, *Sol. Phys.*, 181, 363–394.

Robinson, P. A., and I. H. Cairns (1998b), Fundamental and harmonic emission in type III solar radio bursts. part II: Dominant modes and dynamic spectra, *Sol. Phys.*, 181, 395–428.

Robinson, P. A., A. J. Willes, and I. H. Cairns (1993), Dynamics of Langmuir and ion-sound waves in type III solar radio sources, *Astrophys. J.*, 408, 720–734.

Röttgering, H., M. van Haarlem, and G. Miley (2005), LOFAR-A new low-frequency radio telescope, in *IAU Colloq. 199: Probing Galaxies Through Quasar Absorption Lines*, edited by P. Williams, C.-G. Shu and B. Menard, pp. 381–386, Cambridge Univ. Press, Shanghai, doi:10.1017/S1743921305002851.

Salah, J. E., C. J. Lonsdale, D. Oberoi, R. J. Cappallo, and J. C. Kasper (2005), Space weather capabilities of low frequency radio arrays, in *Solar Physics and Space Weather Instrumentation*, edited by S. Fineschi, and R. A. Viereck, *Proc. SPIE*, 5901, 124–134, doi:10.1117/12.613448.

Schmidt, J. M. (2000), Flux ropes embedded in a radial magnetic field: Analytic solutions for the external magnetic field, *Sol. Phys.*, 197, 135–148.

Schmidt, J. M., and P. J. Cargill (2000), A model for accelerated density enhancements emerging from coronal streamers in Large-Angle and Spectrometric Coronagraph observations, *J. Geophys. Res.*, 105, 10,455–10,464.

Schmidt, J. M., and P. J. Cargill (2001), Magnetic cloud evolution in a two-speed solar wind, *J. Geophys. Res.*, 106, 8283–8290.

Schmidt, J. M., and P. J. Cargill (2003), Magnetic reconnection between a magnetic cloud and the solar wind magnetic field, *J. Geophys. Res.*, 108(A1), 1023, doi:10.1029/2002JA009325.

Schmidt, J. M., and P. J. Cargill (2004), A numerical study of two interacting coronal mass ejections, *Ann. Geophys.*, 22, 2245–2254.

Sheeley, N. R., R. A. Howard, M. J. Koomen, D. J. Michels, R. Schwenn, K. H. Mühlhäuser, and H. Rosenbauer (1985), Coronal mass ejections and interplanetary shocks, *J. Geophys. Res.*, 90, 163–175.

Sheeley, N. R., et al. (1997), Measurements of flow speeds in the corona between 2 and 30 $R_\odot$, *Astrophys. J.*, 484, 472–478.

St. Cyr, O. C., et al. (2000), Properties of coronal mass ejections: SOHO LASCO observations from January 1996 to June 1998, *J. Geophys. Res.*, 105, 18,169–18,186.

Vourlidas, A., D. Maia, M. Pick, and R. A. Howard (1999), LASCO/Nançay observations of the CME on 20 April 1998: White light sources of type II radio emission, in *Magnetic Fields and Solar Processes. The 9th European Meeting on Solar Physics*, Held 12 –18 September , 1999, in Florence, Italy, edited by A. Wilson, pp. 1003–1007, *Eur. Space Agency, ESA SP–448*, ESA Commun. Prod. Off., ESTEC, Noordwijk, Netherlands.

Vrsnak, B., H. Aurass, J. Magdalenic, and N. Gopalswamy (2001), Band-splitting at coronal and interplanetary type II bursts. Basic properties, *Astron. Astrophys.*, 377, 321–329.

Zalesak, S. T. (1979), Fully multidimensional flux-corrected transport algorithms for fluids, *J. Comput. Phys.*, 31, 335–362.

_____

N. Gopalswamy and J. M. Schmidt, NASA Goddard Space Flight Center, Solar System Exploration, Code 695, 8800 Greenbelt Road, Greenbelt, MD 20771, USA. (gopals@ssedmail.gsfc.nasa.gov; jschmidt@ssedmail.gsfc.nasa.gov)